Bioinspired All-in-One Wound Dressing: Integrating Photothermal-Enhanced Drainage and Strain-Sensing Monitoring for Intelligent Healing

Dapeng Yang

yangdapeng@uhrs.edu.cn

University of Health and Rehabilitation Sciences

Zhihua Liu

University of Health and Rehabilitation Sciences

Naiqian Zhang

University of Health and Rehabilitation Sciences

Tianjia Jiang

University of Health and Rehabilitation Sciences

Cheng Wang

Hong Kong Baptist University

Hui Zheng

Fujian Medical University Union Hospital

Lin Lin

Fudan University Huashan Hospital

Na Li

University of Health and Rehabilitation Sciences

Article

Keywords: Biomimetic asymmetric Janus nanofiber membrane, Wound monitoring, Unidirectional fluid drainage, Photothermal antimicrobial, Skin wound repair

Posted Date: November 11th, 2025

DOI: https://doi.org/10.21203/rs.3.rs-8000117/v1

Additional Declarations: There is **NO** Competing Interest.

Abstract

The effective management of chronic infected wounds faces multiple challenges such as fluid accumulation, easy recurrence of infection, and slow healing process. The core difficulty lies in achieving efficient fluid drainage and continuous antibacterial action. Inspired by the asymmetrical wetting property of the Pistia stratiotes, this study designed a biomimetic asymmetric double-layer electrospun nanofiber membrane, integrating one-way drainage, photothermal enhanced evaporation, antibacterial and strain-sensing functions to promote chronic wound healing. This membrane is composed of the upper layer of hydrophilic polyurethane modified with tannic acid-iron-AgNWs complex (PU-xTA/Fe^{3+}/xAg) and the lower layer of hydrophobic PU. Through the gradient of wetting property induced by interface contact, the liquid can be directly pumped from the hydrophobic layer to the hydrophilic layer within 10 s. Moreover, the TA/Fe^{3+} complex in the hydrophilic layer endows the material with excellent photothermal properties, enabling rapid evaporation of secretions and irreversible damage to bacteria, thereby effectively inhibiting infection, reducing inflammation, and promoting fibroblast activity and wound repair. Animal experiments showed that the wound treated with this nanofiber membrane had a healing rate of up to 94.6%. Additionally, combined with the conductive network of deposited silver nanowires, this nanofiber membrane possesses a wide strain range (160%), high sensitivity (gauge factor 7399), rapid response (< 400 ms), which can continuously monitor body surface movement and issue warnings when the wound undergoes excessive deformation. This study provides an intelligent scaffold solution integrating drainage, antibacterial properties, wound healing promotion, and real-time monitoring for the comprehensive management of chronic infected wounds, demonstrating significant clinical translation potential.

1. Introduction

The healing and repair of chronic wounds remain a major clinical challenge worldwide and continue to draw the attention of researchers in the field of public health[1, 2, 3, 4, 5]. Such wounds, due to their difficulty in healing, not only cause significant pain to patients but also result in high medical costs, becoming a heavy burden on the global healthcare system[6, 7, 8]. Ideal wound healing depends on a precise balance of a moist microenvironment: excessive exudate can infiltrate and damage the surrounding healthy tissues, and at the same time, it is prone to induce bacterial infections[9]. However, overly dry wounds can impede the migration of cells and the epithelialization repair process, leading to delayed healing[10]. Therefore, effective exudate management and bacterial infection control are the two most core challenges faced in the clinical process of promoting wound healing.

To address these challenges, a variety of advanced treatment strategies and wound dressings have been developed in recent years, including hydrogels[11, 12, 13], sponges[14, 15], and electrospun nanofiber scaffolds[16, 17], etc. These materials are dedicated to providing a superior moist environment and anti-infection ability compared to traditional dressings. Despite this, the existing strategies still have obvious limitations. The primary issue lies in its single function[18, 19]. The design of most dressings mainly

focuses on a single function in the absorption of exudate or the release of antibacterial agents, making it difficult to address multiple obstacles such as exudate and infection in a coordinated manner[20]. Secondly, traditional antibacterial strategies that rely on antibiotics or metal ions not only face increasingly severe challenges of drug resistance, but their modes of action are also mostly passive and slow[21, 22]. More crucially, the existing dressings generally lack the ability to monitor and provide feedback on the condition of wounds in real time[23, 24]. They cannot provide clinicians or patients with key information about the status of exudate, local physiological parameters, or mechanical traction of the wound due to physical activity, which is crucial for avoiding secondary injuries, achieving personalized and precise care, and assessing the progress of healing[25, 26, 27, 28].

In response to the above challenges, this study developed an integrated intelligent wound dressing platform. Inspired by the natural design of Pistia stratiotes, which uses superhydrophobic leaves and hydrophilic roots to achieve stable floating and effective water control, we have constructed an asymmetric Janus nanofiber membrane. The design of this platform is mainly based on the following three core functions: Firstly, by constructing an asymmetric Janus structure, it achieves active and directional seepage management capabilities[4, 29, 30]. This structure can effectively direct excessive wound exudate from the wound surface to the outside and promote evaporation, thereby maintaining a suitable moist environment locally at the wound site, avoiding tissue impregnation and reducing the risk of infection[31, 32]. Secondly, introduce a powerful photothermal antibacterial strategy with on-demand activation to combat infection[33, 34]. By irradiating with NIR light, the temperature at the wound site rises, achieving a rapid and broad-spectrum sterilization effect, and it is less likely to induce bacterial resistance[35, 36, 37]. In addition, photothermal therapy (PTT) can also promote the acceleration of angiogenesis and cellular metabolism through thermal effects, thereby synergistically promoting wound repair[38]. Finally, integrate real-time strain sensing functions to monitor the mechanical status of the wound[39]. This sensor can sensitively respond to deformations at the wound site caused by joint movements, etc., and monitor and record in real time abnormal pulling activities that may lead to secondary injuries. For patients with reduced sensory function or confusion, this function can provide crucial motor data support for clinical care, thereby achieving early injury warning and personalized activity management[39, 40, 41].

Specifically, in this study, an asymmetric Janus-type double-layer nanofiber membrane was fabricated using electrospinning technology. The upper layer is composed of a photothermal composite formed by the coordination of TA with Fe^{3+}, which possesses both hydrophilicity and efficient photothermal antibacterial properties. By introducing silver nanowires (AgNWs), a hydrophilic sensing network with high conductivity and sensitive response characteristics was constructed. The lower layer is based on PU, providing mechanical support and a hydrophobic barrier function. The experimental design route is shown in Fig. 1. We systematically evaluated the excellent performance of this dressing in aspects such as liquid drainage, photothermal antibacterial, real-time sensing, and biocompatibility, and further verified its significant promoting effect on wound healing in a rat infected wound model. Additionally, based on

in-depth analysis of single-cell RNA sequencing, the potential molecular mechanism of this dressing in regulating the wound microenvironment and accelerating the repair process was revealed. This study not only developed a class of highly performing multifunctional wound dressings, but more importantly, provided new ideas and paradigms for achieving a "smart" and personalized medical model that integrates both monitoring and treatment functions.

2. Experimental Section

2.1. Synthesis of PU-TA/Fe^{3+}/Ag@PU nanofiber membrane.

Firstly, 2 g of PU was dissolved in a mixture of 4 mL tetrahydrofuran and 4 mL N, N-dimethylformamide. The solution was thoroughly stirred to form a homogeneous mixture. Then, TA was added to the solution at mass ratios of 0%, 0.5%, 1.5%, 2.5%, and 3%, and the mixture was continuously stirred until TA was completely dissolved. The resulting solution was injected into an electrospinning device, and electrospun under a positive voltage of 15 kV and a receiving distance of 15 cm, to obtain a PU-TA composite nanofiber membrane. Subsequently, the fiber membrane was placed in a 60°C oven for drying for 2 h, then immersed in a ferric chloride solution for 12 h to form a TA/Fe^{3+} coordination structure. After the reaction, the membrane layer was rinsed with ultrapure water and dried again at 60°C to obtain a PU-xTA/Fe^{3+} nanofiber membrane. Next, the above membrane material was immersed in an AgNWs dispersion solution and ultrasonicated for 1, 5, and 10 min respectively to introduce different loading amounts of AgNWs on the fiber surface, to construct a conductive network, and obtain a PU-xTA/Fe^{3+}/xAg composite nanofiber membrane. Finally, PU electrospinning was performed on the surface of this membrane layer to form an asymmetric Janus nanofiber membrane.

2.2. Characterization of Janus nanofiber membranes

The crystal structures of the PU-xTA/Fe^{3+} and PU-xTA/Fe^{3+}/xAg@PU Janus nanofiber membranes were evaluated using XRD (Bruker D8 Advance, Germany), with the measurement range of 2θ from 5–80 °, a scanning step rate of 1.8 °/min, a power of 2.2 kW, a working voltage of 40 kW, and a working current of 40 mA. Subsequently, Fourier transform infrared spectroscopy (FT-IR; Thermo Scientific, USA) was used to analyze the chemical bonds and functional groups of the PU-xTA/Fe^{3+} nanofiber membranes within the range of 4000 – 400 cm^{-1}. Subsequently, scanning electron microscopy (SEM) was used to study the surface morphology and fiber diameters of the PU-xTA/Fe^{3+} and PU-xTA/Fe^{3+}/xAg@PU Janus nanofiber membranes. Then, X-ray photoelectron spectroscopy (XPS) was used to analyze the surface electronic state and elemental composition of the PU-2.5TA/Fe^{3+}/1Ag@PU Janus nanofiber membranes. Zeta potential and particle size were measured using Zeta potential and particle size analyzer (Malvern Instruments, UK) for the AgNWs. In addition, the elasticity of the nanofiber membranes is also an important indicator for wound repair materials, so a universal tensile machine was used for mechanical strength testing. To verify the hydrophilicity and hydrophobicity of the materials, water contact angle tests were conducted on the PU-xTA/Fe^{3+} and PU-2.5TA/Fe^{3+}/1Ag@PU Janus nanofiber membranes.

The water vapor transmission rate (WVTR) of the PU-2.5TA/Fe^{3+}/1Ag was determined using a dedicated instrument (C360M, Labthink).

3. Results and Discussion

3.1. Characterization of the PU-xTA/Fe^{3+}/xAg

The schematic diagram of the preparation of Janus nanofiber membranes is shown in Fig. 2a. To verify that the PU-xTA/Fe^{3+} nanofiber membranes were successfully prepared, XRD tests were conducted on them, and the test results are presented in Figure S1. A distinct steamed bun peak appears at 17.3°, and this characteristic peak is a typical sign of the amorphous structure of PU materials. However, as the contents of TA and Fe^{3+} increase, no characteristic peaks belonging to TA and Fe^{3+} are observed. This is because they have formed an amorphous structure. In addition, XRD tests were also conducted on the PU-2.5TA/Fe^{3+}@PU-xAg (x = 1, 5, 10) Janus nanofiber membranes, and the test results are shown in Fig. 2b. The results show that as the content of AgNWs increases, the peak value at 38.3° gradually increases, which proves that AgNWs has been successfully loaded onto the nanofiber membrane. Subsequently, the FT-IR test was conducted to confirm the successful preparation of the PU-xTA/Fe^{3+} nanofiber membrane. The results were shown in Figure S2. The broad absorption peak in the range of 3600 – 3100 cm^{-1} represents the stretching vibration of the phenolic hydroxyl groups in TA. After the reaction with Fe(III), the intensity of the adsorption peak at this position decreases for the product TA-Fe(III); meanwhile, the absorption peak of the C-O stretching vibration connected to the benzene ring in the TA molecule shifts from 1320 cm^{-1} (TA) to 1334 cm^{-1} (TA-Fe(III)), indicating that Fe(III) has coordinated with the phenolic hydroxyl groups of TA. Affected by the coordination effect, the characteristic absorption peaks of the benzene ring in TA at 1500 – 700 cm^{-1} all shift towards lower wavenumbers[42, 43].

Figure S3a shows the full XPS spectrum of the PU-2.5TA/Fe^{3+}/1Ag@PU Janus nanofiber membrane, which further indicates the presence of C, O, N, Fe and Ag in the material, proving the successful preparation of the PU-xTA/Fe^{3+}/xAg@PU Janus nanofiber membrane. The Ag 3d spectrum (Fig. 2c) shows a double peak with binding energies at 367.4 eV (Ag $3d_{5/2}$) and 373.5 eV (Ag $3d_{3/2}$), and the spin-orbit splitting interval is approximately 6 eV. Further peak-fitting of the Ag $3d_{5/2}$ peak can distinguish Ag^{+} and Ag^{0} species, confirming the presence of elemental silver[44]. Figure S3b shows the C 1s spectrum, with three fitting peaks visible, corresponding respectively to the C-C (284.8 eV), C-O-C (285.3 eV), and O-C = O (286.4 eV) functional groups. Figure S3c shows the O 1s spectrum. The peaks at 531.7 eV, 530.8 eV and 532.6 eV can be respectively attributed to the contributions of C-O, C = O and O-H. The N 1s spectrum (Figure S3d) shows characteristic peaks at 399.3 eV and 400.4 eV, respectively derived from C-N and N-H bonds. In the Fe 2p spectrum (Figure S3e), characteristic peaks corresponding to Fe $2p_{3/2}$ and Fe $2p_{1/2}$ were observed at 710.9 eV and 722.7 eV respectively, and corresponding satellite peaks appeared at 715.8 eV and 733.2 eV, indicating that the iron element mainly exists in the form of Fe^{3+}.

Figure 2d shows the variation of the water contact angle of different PU-xTA/Fe^{3+} nanofiber membranes. The water contact angle of the pure PU nanofiber membrane is 118°, which proves that the pure PU membrane has strong hydrophobicity. With the increase of TA concentration in it, the PU-xTA/Fe^{3+} nanofiber membrane gradually becomes hydrophilic. When the content of TA is increased to 1.5%, the water contact angle of the nanofiber membrane has become 0°. This also proves that with the increase of TA content, the PU-xTA/Fe^{3+} nanofiber membrane undergoes a rapid transformation from hydrophobic to hydrophilic. Moreover, after ultrasonic treatment of AgNWs, the PU-2.5TA/Fe^{3+}/1Ag nanofiber membrane also exhibits hydrophilicity.

The SEM image in Fig. 2e reveals the microstructure of the nanofiber membrane, showing fibers with a uniform and randomly oriented distribution. As illustrated in Figure S4, the fiber diameters in the PU-xTA/Fe^{3+} (x = 0, 0.5, 1.5, 2.5, 3) samples mainly range from 0.02 to 0.24 μm, with the majority concentrated around 0.12 μm. With the increase of TA content, there was no significant change in the morphology and diameter of the fibers, indicating that the addition of TA has a limited impact on the fiber structure. Furthermore, as the ultrasonication time of the PU-2.5TA/Fe^{3+} nanofiber membrane in the AgNWs suspension increased, the amount of AgNWs attached to its surface gradually rose. The AgNWs exhibited a short rod-like structure, with lengths approximately between 1–3 μm, and were intermittently and uniformly distributed on the fiber surface. This morphological characteristic was further confirmed by the particle size analysis of the AgNWs (Figure S5). The Zeta potential of AgNWs is 17 eV (Figure S6), which also indicates that they have excellent dispersibility. EDS mapping analysis of the PU-2.5TA/Fe^{3+}/1Ag sample showed that elements such as C, O, N, Fe, and Ag were uniformly distributed in the Mapping image (Fig. 2f), and the elemental signals closely aligned with the orientation of the electrospun fibers, indicating good dispersion and structural consistency of the functional components within the fiber membrane. In addition, the interior of the nanofiber membrane forms pores of various sizes. This porous characteristic helps to enhance its breathability when used as a skin wound dressing. To further evaluate this performance, we measured the WVTR of the PU-2.5TA/Fe^{3+}/1Ag@PU using a dedicated instrument, and the result was 1079.24 g/(m^2·day). This WVTR value can effectively prevent excessive evaporation of the membrane's own moisture and achieve efficient liquid transport under the effect of photothermal regulation. As shown in Figure S7, the macroscopic water vapor transmission experiment further verified the excellent breathability of the PU-2.5TA/Fe^{3+}/1Ag@PU nanofiber membrane.

3.2. Photothermal performance testing and fluid drainage performance of nanofiber membranes

To achieve effective drainage of wound exudate and maintain moderate dryness of the wound, this study designed a double-layer nanofiber membrane with the function of fixating and guiding fluid. As shown in Fig. 3a-c, due to the good hydrophilicity of the upper PU-xTA/Fe^{3+}/xAg nanofiber membrane and the strong hydrophobicity of the lower PU nanofiber membrane, when water droplets are placed above the hydrophilic layer, they are effectively locked within this layer within 20 s. On the contrary, if the

hydrophobic layer is placed on the upper layer and the hydrophilic layer on the lower layer, due to the suction effect of the hydrophilic structure on the lower layer, water droplets will be rapidly sucked to the hydrophilic layer within 10 s. To further verify its fluid guiding ability, water droplets were directly brought into contact with the lower hydrophobic film. It could be seen that the liquid was rapidly drawn to the upper hydrophilic layer, and the upward transfer of the liquid was completed within 15 s. The corresponding test videos for the fluid drainage experiment are shown in Figures S8, S9, and S10. The result indicates that the constructed biomimetic asymmetric Janus nanofiber membrane has excellent unidirectional fluid guide performance and has potential application value in wound exudate management.

As a widely used photothermal material, the excellent photothermal conversion performance of Fe^{3+}-based materials has been extensively studied and verified. As shown in Fig. 3d-f, in the dry state, with the increase of TA content in the upper nanofiber membrane, the content of Fe^{3+} complexed by it also increases accordingly. Under the irradiation of 808 nm NIR (1.5W/cm^2) light, the heating rate of the material gradually increases, and the equilibrium temperature also gradually rises. Among them, the equilibrium temperature of the PU-3TA/Fe^{3+} group was the highest, reaching 117°C. However, in the PU-0TA/Fe^{3+} group, the temperature hardly changed significantly throughout the entire illumination process, indicating that there was almost no photothermal response. To simulate the exudate environment of a real wound, we conducted photothermal performance tests on the nanofiber membrane in a moist state (Fig. 3g-i). The results show that the equilibrium temperatures of all samples in a moist state are lower than those in a dry state. It is worth noting that the PU-3TA/Fe^{3+} sample briefly reached 63°C after 120 s of irradiation. At this time, the film layer was basically dry, and the temperature rose further if the irradiation continued. Figure S11 shows the photothermal heating behavior of the same nanofiber membrane under near-infrared light of different power densities. Under dry conditions, as the NIR laser power density increased from 0.5 W/cm^2 to 1 W/cm^2, the equilibrium temperature rose significantly from 44.0 ± 0.2°C to 67.5 ± 0.2°C, demonstrating the excellent photothermal responsiveness of the material. It is worth noting that under wet conditions (Figure S12), the temperature rise was initially moderated by water evaporation; however, once the moisture was largely evaporated, a second temperature increase was observed until a stable equilibrium was reached. This indicates that the laser power has an impact on the photothermal performance. To further evaluate the photothermal stability of the material, three cycles of photothermal experiments were conducted on PU-2.5TA/Fe^{3+} nanofiber membranes (Figure S13). Its equilibrium temperature is always maintained at 100 ± 2°C, which is consistent with the results of the aforementioned photothermal experiment, indicating that the material has good reusability.

Based on the photothermal properties exhibited by the PU-xTA/Fe^{3+} material, we speculate that its unidirectional water transport capacity can be further enhanced through the photothermal induced evaporation mechanism. To verify this hypothesis, we first used PU-2.5TA/Fe^{3+}/10Ag@PU nanofiber membranes as the test material, placed them on the water surface and exposed them to 808 nm laser irradiation for 60 min, and monitored the changes in drainage quality in real time (Fig. 3j). The results (Fig. 3k) show that in the absence of light, the evaporation rate of the film is only 0.0125 g·cm^{-2}. This

indicates that the evaporation is mainly caused by the heat exchange between the nanofiber membrane and the environment. Under light conditions, the evaporation significantly increased to 0.54 $g \cdot cm^{-2}$, indicating that the photothermal effect, as an external driving force, effectively enhanced the directional transport and evaporation of water. To further determine the contribution of liquid conduction performance and photothermal effect, we inverted the membrane to the PU@PU-2.5TA/Fe^{3+}/10Ag structure for a control experiment. The evaporation of this structure under light is 0.31 $g \cdot cm^{-2}$, which is significantly lower than that of the upright configuration. Furthermore, the evaporation rate analysis (Fig. 3l) indicates that the evaporation rate of the upright membrane with a liquid-conducting structure is approximately twice that of the inverted structure. This further confirms that this biomimetic asymmetric Janus structure and TA/Fe^{3+} have played a crucial role in achieving efficient directional water transport.

To further explore the influence of material composition on evaporation performance, we conducted systematic tests on PU-xTA/Fe^{3+} (x = 0, 0.5, 1.5, 2.5) nanofiber films with different TA contents. The results (Figure S14) showed that as the TA content increased from 0% to 2.5%, the cumulative evaporation water volume gradually rose, and the PU-2.5TA/Fe^{3+} group reached the maximum value of approximately 0.59 $g \cdot cm^{-2}$, indicating that the coordination degree of TA/Fe^{3+} was positively correlated with the photothermal conversion efficiency. The results of water evaporation rate (Figure S15) further indicated that the stable evaporation rate of the PU-2.5TA/Fe^{3+} group was the highest (approximately 0.6 $g \cdot cm^{-2} \cdot h^{-1}$), suggesting that it had the most excellent and sustained water evaporation capacity. The evaporation effect induced by photothermal can effectively maintain the interface of the dressing in an unsaturated state, thereby ensuring the continuous discharge of wound exudate. This study provides important experimental evidence for the development of intelligent dressings that have both active liquid conduction and photothermal enhancement functions in wet environments.

Additionally, to explore the intrinsic electrical mechanism of the differences in photothermal conversion performance, we further tested the photocurrent response and AC impedance of the materials. As shown in Figure S16, under periodic illumination, all samples produced rapid response transient photocurrents, and their intensities significantly increased with the increase in the proportion of TA. The PU-0TA/Fe^{3+} group could only detect a weak background signal, while the photocurrent intensity of the PU-2.5TA/Fe^{3+} group was approximately four times that of the PU-0.5TA/Fe^{3+} group. This clearly indicates that the coordination complex formed by TA and Fe^{3+} is the main photoreactive center, and the high TA content effectively promotes the generation and separation of more photogenerated carriers, providing sufficient energy for efficient photothermal conversion. At the same time, the Nyquist impedance spectrum (Figure S17) results are highly consistent with the photocurrent data. As the proportion of conductive filler increases from 0% to 2.5%, the radius of the capacitive arc in the impedance spectrum decreases to one quarter of its original value, indicating that the charge transfer impedance of the material gradually decreases. This enhanced electrical conductivity characteristic not only directly manifests as a stronger photocurrent signal, but also optimizes the conversion efficiency of light energy to heat energy by increasing the probability of non-radiative recombination.

3.3. Motion sensing detection *in vitro*

The strain-dependent resistive response of the PU-2.5TA/Fe^{3+}/xAg (x = 1, 5, 10) nanofiber membranes was systematically investigated through tensile testing. Their sensitivity profiles are presented in Fig. 4a-c. The incorporation of AgNWs into the TA/Fe^{3+} crosslinked PU matrix not only enhanced electrical conductivity but also effectively modulated the dynamic evolution of the conductive network under strain. At a lower Ag content (x = 1), the composite formed a stable yet sparse conductive network, exhibiting a highly linear response with a gauge factor (GF) of 19 in the 0–20% strain range. The material remained responsive even in the microstrain regime (0–1%), enabling reliable detection of subtle deformations such as those induced by pulse or breathing. This makes it suitable for quantitative monitoring of strain distribution across wound areas. With the further increase of strain, the sensitivity gradually increases, and GF rises from 177 to 490, showing obvious space-dependent sensing behavior. With higher Ag loading (x = 5 and 10), the strain sensing range extended beyond 0-180%, and the sensitivity in high-strain regions increased markedly. This enhancement stems from the AgNWs facilitating cooperative slipping and separation of conductive pathways during stretching, resulting in an exponential rise in resistance. Notably, at 150–180% strain, the x = 10 composite achieved an exceptional GF of 7399. This performance can detect extreme mechanical deformations, such as those caused by large-angle joint flexion or tissue swelling, which lays the foundation for it to perform continuous and stable monitoring tasks in real and variable physiological environments. Collectively, the materials exhibited progressively enhanced sensitivity across multiple strain intervals while maintaining excellent linearity even at high strains. This demonstrates their stable sensing performance under varying mechanical stimuli-from subtle physiological signals to large-scale body movements. By tailoring the Ag content, we have optimized the strain-responsive behavior of the material, providing an effective design strategy for flexible sensors suited to full-range biomechanical monitoring.

The cyclic stability of the sensor was further evaluated under periodic mechanical stimuli simulating different human joint movements. As shown in Fig. 4d-f, with all three subplots depicting the relative resistance change over time to reflect the sensor's reproducible response under dynamic biomechanical loading. When subjected to finger joint bending, the resistance varied periodically within a moderate range of approximately 150%, exhibiting consistent "peak–valley" patterns over multiple cycles under both 30° and 60° bending angles, which demonstrates excellent signal reproducibility under low to moderate strain and suggests suitability for monitoring subtle and frequent movements. For the detection of wrist flexion, the resistance variation range has significantly increased by more than 900%. It maintained stability and repeatability throughout the entire cycle without signal attenuation, confirming its excellent reliability even under large strains caused by wrist joint movement. Further, under high-angle elbow joint bending, the signal retained high stability despite minor oscillations, highlighting the sensor's ability to adapt to varying strain amplitudes within a single monitoring session. This experiment demonstrated the potential of sensors in long-term wearable health monitoring, especially in the assessment of joint recovery and motion tracking during wound healing.

The resistive response of the PU-2.5TA/Fe^{3+}/10Ag nanofiber membrane was further investigated under varying tensile speeds (10–200 mm/min at 10% strain) and strain levels (1-100% at 200 mm/min). Data revealed that neither tensile speed nor strain magnitude significantly influenced the sensing output, confirming the reliability and accuracy of the sensor, as well as its ability to continuously detect both subtle and large strains (Fig. 4g, h). Furthermore, the response speed was evaluated, as shown in Fig. 4i. The sensor exhibited a response time of 400 ms, demonstrating its capacity for rapid recognition of high-frequency strain signals.

To evaluate the sensor's durability and operational stability, 50 min stretch-release cyclic tests were conducted under 50% strain at a tensile rate of 50 mm/min (Fig. 4j). The resistive response exhibited dense and highly consistent periodic "peak–valley" fluctuations, with the amplitude and frequency remaining stable throughout the entire testing period, showing no noticeable signal decay. To further validate the consistency of the response, two representative time windows (around 700 s and 2750 s) were selected for detailed local analysis. The enlarged views clearly demonstrate that the waveform characteristics, peak amplitude, and response period in both segments align closely with each other, without any distortion or signal degradation. These results conclusively confirm the excellent response repeatability and structural durability of the sensor under long-term dynamic strain, underscoring its reliability for continuous monitoring applications such as human motion tracking or prolonged physiological signal detection.

3.4. The performance of photothermal antibacterial effect

The antibacterial efficacy of PU-xTA/Fe^{3+} (x = 0, 0.5, 1.5, 2.5) nanofiber membranes under NIR light irradiation was evaluated against both *S. aureus* and *E. coli*. As shown in Fig. 5a, b, the membranes containing 1.5 and 2.5 TA achieved bactericidal rates exceeding 95% after only 5 min of NIR irradiation. Remarkably, complete sterilization (100% bactericidal rate) was observed within 10 min of exposure (Fig. 5d1, d2). These results clearly indicate that the PU-xTA/Fe^{3+} nanofiber membrane has excellent photothermal antibacterial properties. Furthermore, five cycles of antibacterial experiments were repeatedly conducted on PU-2.5TA/Fe^{3+} nanofiber membranes. The experimental results (Figure S18) proved that the antibacterial rate was close to 100% each time, demonstrating that PU-xTA/Fe^{3+} nanofiber membrane has excellent reusability.

To explore the damage mechanism of bacteria after antibacterial treatment, we observed the bacterial morphology using FE-SEM (Fig. 5c). The results showed that after treatment with PU-0TA/Fe^{3+} and irradiation for 5 min, *S. aureus* and *E. coli* still maintained intact cell morphology, with smooth surfaces and no rupture of cell membranes, indicating that this group of materials did not have obvious antibacterial properties. In contrast, after treatment with PU-2.5TA/Fe^{3+} and irradiation for the same period of time, both types of bacteria showed obvious deformation, contraction and cell membrane rupture, and even intracellular substance leakage, indicating that this group of materials caused severe damage to the bacterial structure.

To further reveal its antibacterial mechanism, we further evaluated the changes in bacterial membrane permeability through the hydrolysis experiment of ONPG (Figs. 5e1, e2). When the permeability of the bacterial membrane increases, ONPG enters the cell and is hydrolyzed by β -galactosidase, resulting in an increase in absorbance at 420 nm. The absorbance (OD value) of the control group and the PU-0TA/Fe^{3+} group did not change significantly after NIR illumination, indicating that the membrane permeability did not change significantly. The OD value of the PU-2.5TA/Fe^{3+} group significantly increased to 0.31 after light exposure, confirming that the photothermal effect could enhance the permeability of the bacterial membrane and cause irreversible damage. The destruction of the membrane structure further led to the leakage of intracellular proteins[45, 46]. We quantified the protein leakage situation by the BCA method (Figs. 5f1, f2). Compared with the control group and the PU-0TA/Fe^{3+} group, the OD value of the PU-2.5TA/Fe^{3+} group was the highest (up to 0.23), indicating the most severe protein leakage. This result was consistent with the SEM observation.

The above results indicate that PU-2.5TA/Fe^{3+} can effectively kill bacteria due to its excellent photothermal conversion ability and iron ion release effect. The mechanism also includes the generation of reactive oxygen species (ROS), which causes oxidative stress damage. We used the DCFH-DA fluorescent probe to detect the ROS level in the bacteria (Figs. 5g1, g2). It was found that the OD value of PU-2.5TA/Fe^{3+} group increased to 6.5×10^6 after 5 min of light, indicating that this group had the largest ROS production. This result further explains the antibacterial performance of the material from the perspective of oxidative damage. To clarify the specific types and generation mechanisms of the generated ROS, we further analyzed them using electron spin resonance (ESR) spectra (Fig. 5h-j). The results show that PU-2.5TA/Fe^{3+} can generate various ROS during the photocatalytic process, including singlet oxygen ($^1O_2$), hydroxyl radicals (·OH), and superoxide anions ($\cdot O_2^-$). Moreover, as the duration of light exposure increases, the peak intensity of ESR becomes more pronounced. These highly active oxides can efficiently destroy the cellular structure of bacteria and interfere with their metabolic processes, thereby synergistically exerting photothermal effects to achieve highly effective antibacterial effects[47]. The above-mentioned antibacterial mechanism demonstrates the good application potential of PU-2.5TA/Fe^{3+} in the anti-infection treatment of skin wounds.

3.5. *In vitro* biocompatibility evaluation

Biocompatibility is a fundamental requirement for designing tissue engineering scaffolds and promoting wound healing. To assess the biocompatibility of the PU-2.5TA/Fe^{3+}/xAg@PU nanofiber membrane, a 7-day cytotoxicity test was conducted using L929 cells. As illustrated in Figs. 6a–c, after normalization, the groups containing PU-2.5TA/Fe^{3+}/xAg@PU (x = 1, 5, 10) not only exhibited no cytotoxicity but also significantly promoted cell proliferation on days 1, 3, and 7. To visually evaluate cell viability, live/dead staining was performed after 72 hours of culture. The results revealed a higher cell density in the treatment groups compared to the control (Fig. 6d), indicating that the material surface favors cell attachment and spreading.

The *in vitro* scratch wound assay, which partially mimics the *in vivo* wound healing process, provides valuable insight into the reparative performance of the materials. As shown in Fig. 6e, the wound closure rate increased with higher silver ion concentrations in the PU-2.5TA/Fe^{3+}/xAg@PU (x = 1, 5, 10) nanofiber membranes. The PU-2.5TA/Fe^{3+}/10Ag@PU group demonstrated the fastest repair rate, with wound healing nearly reaching 100% of the control group by 36 h (Fig. 6f). In contrast, the healing rates of the PU-2.5TA/Fe^{3+}/1Ag@PU and 5Ag groups were comparable. Notably, all groups exhibited the highest repair rate between 24–36 h.

Hemocompatibility was evaluated via a hemolysis assay using mouse blood. The positive control showed a red supernatant due to severe hemolysis, whereas the test groups displayed only a slight reddish hue with clear supernatant and intact erythrocytes (Fig. 6g). Quantitative analysis confirmed that the hemolysis rates of each material group were all below 0.58%, all below the safety threshold of 5%[48], proving that the PU-2.5TA/Fe^{3+}/xAg@PU nanofiber membrane has good blood compatibility. Additionally, hemolysis tests performed on PU-xTA/Fe^{3+} (x = 0%, 0.5%, 1.5%, 2.5%, 3%) nanofiber membrane revealed a maximum hemolysis rate of only 1.27% relative to the positive control (Figure S19), further supporting the outstanding blood compatibility of the material system and its suitability for biomedical applications.

3.6. *In vivo* validation

Previous *in vitro* experiments demonstrated that the PU-2.5TA/Fe^{3+}/xAg@PU nanofiber membrane exhibited excellent performance in maintaining wound drainage, breathability, and promoting wound healing in vitro. To further evaluate its *in vivo* efficacy, we established a full-thickness skin defect rat model with Staphylococcus aureus infection (Fig. 7a). After photothermal treatment of rats, their thermal imaging images are shown in Fig. 7b. In the control group, the wound temperature increased from 33°C to 36.7°C within 210 s, while in the PU-2.5TA/Fe^{3+}/10Ag@PU group, it increased from 34.4°C to 49.6°C (Figure S20), indicating that the membrane also has a certain photothermal capacity on the body surface.

Figure 7c presents representative images of the wounds at different time points (day 0, 3, 6, 10, and 14). On the 3rd day, the control wound had not yet fully scabbed and was accompanied by a small amount of secretion, while the wound covered with the PU-2.5TA/Fe^{3+}/10Ag@PU membrane was relatively dry and had formed a scab, indicating its excellent ability to manage exudate. As time passed, the wound areas of each group gradually decreased. By the 14th day, the control group still had a large unhealed area remaining, while the PU-2.5TA/Fe^{3+}/1Ag@PU group was basically closed, and the PU-2.5TA/Fe^{3+}/10Ag@PU group's wound was nearly completely healed. The simulated healing images are shown in Fig. 7d. Quantitative analysis showed that the latter had a healing rate of up to 94.6% on the 14th day (Fig. 7e). During the skin wound repair cycle of rats, we collected wound exudate on the 3rd and 10th days and conducted bacterial culture. The results showed that compared with the control group, the colony count of the PU-2.5TA/Fe^{3+}/10Ag@PU group was significantly reduced on the 3rd and 10th days

(Fig. 7f, g), indicating that this material still possesses good antibacterial properties in the *in vivo* environment.

Further, the tissue repair status was observed through H&E staining and Masson staining (Fig. 7h, i). In the control group, there was epidermal necrosis, inflammatory exudation, disordered arrangement of granulation tissue, infiltration of inflammatory cells, and loss of skin appendages, indicating poor repair effect. In contrast, the PU-2.5TA/Fe^{3+}/10Ag@PU group had intact epidermal structure, dense arrangement of granulation tissue in the dermis, abundant fibroblasts, mild inflammatory response, and visible new hair follicles, suggesting that it can effectively promote the structural and functional repair of full-thickness skin defects. The Masson results (Fig. 7i) showed that the collagen fibers in the control group were sparse and the staining was relatively light, while the collagen fibers in the PU-2.5TA/Fe^{3+}/10Ag@PU group were dense, the staining was deep blue, and the matrix was uniform without abnormal deposition. Quantitative analysis (Figure S21) revealed that the PU-2.5TA/Fe^{3+}/10Ag@PU group accounted for 60.9%. This proves the role of materials in promoting wound repair.

To deeply elucidate the mechanism of action of the nanofiber membrane with hierarchical drainage, photothermal sterilization and wound healing promotion functions, we collected the wound tissues on the 14th day and conducted RNA sequencing analysis, comparing PU-2.5TA/Fe^{3+}/10Ag@PU, PU-2.5TA/Fe^{3+}/0Ag@PU and the blank control group. The up-regulation results of the gene are shown in Figure S22. Firstly, when comparing PU-2.5TA/Fe^{3+}/0Ag@PU with the control group, we identified 233 up-regulated genes and 97 down-regulated genes (Figure S23). Among them, multiple keratin-related genes such as KRTAP17-1, KRT10, and KRT82 showed significant increases in expression. The proteins encoded by these genes are key components for maintaining the integrity and mechanical strength of epithelial cells, and they jointly participate in the construction of the keratin fiber network, suggesting that the material may provide support for wound re-epithelialization by enhancing the structural stability of epidermal cells. At the same time, the expression of inflammatory-related gene CXCL2 was significantly down-regulated, further confirming the timely resolution of the inflammatory response and creating favorable conditions for tissue repair. KEGG enrichment analysis (Figure S24) showed that the most significant difference pathway between the two groups was the *S. aureus* infection response, which was consistent with the experimental modeling goal. The cluster heatmap (Figure S25) indicated that except for one control group sample which clustered with the experimental group due to individual differences, the remaining samples were clearly distinguished according to the treatment conditions, reflecting the overall impact of material treatment on gene expression patterns.

By further comparing PU-2.5TA/Fe^{3+}/10Ag@PU with PU-2.5TA/Fe^{3+}/0Ag@PU, we observed a more extensive transcriptional reprogramming, with 808 genes upregulated and 810 genes downregulated (Fig. 7j). Multiple key immune regulatory genes such as Tcim, Ats3, and Rgs1 showed a significant upward trend. Tcim is closely related to cell proliferation and differentiation, Ats3 acts as a stress-induced transcription factor that helps coordinate the resolution of inflammation and activate the repair

program, while Rgs1 restricts excessive activation and migration of lymphocytes by negatively regulating the GPCR signaling pathway. The coordinated upregulation of these genes delineates a molecular signature for transitioning from an inflammatory state to a reparative immune microenvironment, providing a mechanistic explanation for the observed phenomena at the histological level. The KEGG pathway enrichment (Fig. 7k) analysis further revealed that the genes were significantly enriched in pathways such as "cytoskeleton in muscle cells" and "Hypertrophic cardiomyopathy". The core biological processes all point to cytoskeleton remodeling and regulation of cell contractility. This result suggests that in the material treatment group, the fibroblasts at the wound site were activated and transformed into contractile myofibroblasts, thereby effectively promoting wound contraction and collagen remodeling. Heatmap analysis (Fig. 7l) also confirmed that the two groups of samples were clearly divided into two clusters based on the gene expression profile, indicating that the addition of silver elements triggered a significant transcriptional response.

In summary, RNA sequencing analysis at the molecular level revealed the synergistic mechanism of the PU-2.5TA/Fe^{3+}/10Ag@PU nanofiber membrane: On the basis of the basic structure (PU-xTA/Fe^{3+}@PU) promoting the expression of epidermal barrier-related genes and enhancing structural stability, the introduction of silver elements further regulated the immune microenvironment, accelerated the resolution of inflammation, and activated the contraction and remodeling functions of fibroblasts, thereby jointly driving high-quality functional wound healing.

4. Conclusion

In summary, inspired by the asymmetric wettability structure of Pistia stratiotes, this study successfully designed and fabricated a bioinspired asymmetric Janus nanofibrous membrane (PU-2.5TA/Fe^{3+}/10Ag@PU). Experimental results demonstrate that the Janus membrane achieves directional liquid transport against gravity within 10 s. Under near-infrared light irradiation, its evaporation rate can reach 0.59 $g \cdot cm^{-2} \cdot h^{-1}$, which is twice the rate of reverse directional drainage. This demonstrates its excellent ability to manage exuded liquid. Regarding photothermal performance, the dried PU-2.5TA/Fe^{3+} nanofibrous membrane rapidly heated to over 95°C within 60 s under NIR irradiation (1.5 W/cm^2), while the hydrated membrane consistently reached 60°C. The membrane maintained high stability over three consecutive photothermal cycles, indicating good reusability potential. Antibacterial tests further confirmed that the material achieves nearly 100% antibacterial rate against both *S. aureus* and *E. coli* within 10 min, while maintaining high antibacterial efficacy through five consecutive usage cycles, demonstrating reliable photothermal antibacterial recyclability. Importantly, the nanofibrous membrane exhibits outstanding real-time strain sensing performance with a response time below 400 ms, adapting to wide ranges of stretching speeds (10–200 mm/min) and stress variations (0-160%), thus effectively monitoring wound deformation caused by joint movement. Animal experiments confirmed that the PU-2.5TA/Fe^{3+}/10Ag@PU nanofibrous membrane group achieved 94.6% wound closure rate by day 14 with NIR assistance. Furthermore, molecular mechanism studies based on RNA sequencing revealed that the dressing shapes a microenvironment conducive to skin regeneration by

regulating key immune and tissue repair-related genes. This research not only developed a dressing that integrates functions such as directional liquid transportation, photothermal enhanced evaporation, on-demand sterilization, real-time strain monitoring, and promotion of wound healing, but also provided a new intelligent medical paradigm integrating "prevention-monitoring-treatment" for the repair of chronic wounds.

Declarations

Declaration of Competing Interests

The authors declare that they have no known competing financial interests or personal relationships that could have appeared to influence the work reported in this paper.

Acknowledgements

This work was financially supported by the Qingdao Natural Science Foundation (25-1-1-257-zyyd-jch, 25-1-1-155-zyyd-jch), the Clinical Research Capability Enhancement Project of University of Health and Rehabilitation Sciences (K2025LC7204), the Natural Science Foundation of Shandong Province, China (ZR2024QE467), and the National Natural Science Foundation of China (52303343), Fujian Research and Training Grants for Young and Middle-aged Leaders in Healthcare.

References

1. Kharaziha M, Baidya A, Annabi N. Rational design of immunomodulatory hydrogels for chronic wound healing. *ADVANCED MATERIALS* **33**, 2100176 (2021).
2. Xin JW*, et al.* A thermogalvanic cell dressing for smart wound monitoring and accelerated healing. *NATURE BIOMEDICAL ENGINEERING*, S41551 (2025).
3. Wang JX, Yang YT, Xu HR, Huang SF, Guo BL, Hu J. All-in-One: A multifunctional composite biomimetic cryogel for coagulation disorder hemostasis and infected diabetic wound healing. *NANO-MICRO LETTERS* **17**, s40820 (2025).
4. Huang XX*, et al.* Silver-catechol dynamic redox chemistry provides hydrogel dressings with sustained antioxidant and antibacterial activity for chronic wound care. *ACS NANO* **19**, 22270-22290 (2025).
5. Dai SY*, et al.* A heterogeneous hydrogel patch with mechanical activity and bioactivity for chronic diabetic wound healing. *BIOMATERIALS* **324**, 123531 (2026).
6. Li M*, et al.* A wearable and stretchable dual-wavelength LED device for home care of chronic infected wounds. *NATURE COMMUNICATIONS* **15**, s41467 (2024).
7. Uberoi A, McCready-Vangi A, Grice EA. The wound microbiota: microbial mechanisms of impaired wound healing and infection. *NATURE REVIEWS MICROBIOLOGY* **22**, 507-521 (2024).

8. Wang CR*, et al.* Wound management materials and technologies from bench to bedside and beyond. *NATURE REVIEWS MATERIALS* **9**, 550-566 (2024).
9. Feng F, Zhao Z, Li J, Huang Y, Chen W. Multifunctional dressings for wound exudate management. *Progress in Materials Science* **146**, 101328 (2024).
10. Wang CR*, et al.* A microfluidic wearable device for wound exudate management and analysis in human chronic wounds. *SCIENCE TRANSLATIONAL MEDICINE* **17**, (2025).
11. Zhang F*, et al.* A dynamically phase-adaptive regulating hydrogel promotes ultrafast anti-fibrotic wound healing. *NATURE COMMUNICATIONS* **16**, (2025).
12. Shu HZ*, et al.* Mechanoregulative hydrogel facilitates rapid scarless healing by self-adaptive control of wound niche at different stages. *SCIENCE ADVANCES* **11**, (2025).
13. Chen X*, et al.* 3D printing of chitosan hydrogel reinforced with tubular nanoclay for hemostasis and infected wound healing. *Bioactive Materials* **54**, 404-422 (2025).
14. Lei XX*, et al.* A self-hygroscopic, rapidly self-gelling polysaccharide-based sponge with robust wet adhesion for non-compressible hemorrhage control and infected wounds healing. *BIOACTIVE MATERIALS* **46**, 311-330 (2025).
15. Xu H*, et al.* Preparation and characterization of a polyurethane-based sponge wound dressing with a superhydrophobic layer and an antimicrobial adherent hydrogel layer. *ACTA BIOMATERIALIA* **181**, 235-248 (2024).
16. Zhang XD*, et al.* Spatiotemporally controlled delivery of biological effectors from nanofiber scaffolds accelerates skin wound healing in porcine models. *SCIENCE ADVANCES* **11**, (2025).
17. Du R*, et al.* Black phosphorus-doped Janus structured electrospun fibrous membrane with antibacterial properties for wound healing. *Chemical Engineering Journal* **519**, 165605 (2025).
18. Sun M*, et al.* Herb-functionalized chronic wound dressings for enhancing biological functions: multiple flavonoids coordination driven strategy. *ADVANCED FUNCTIONAL MATERIALS* **32**, (2022).
19. Guo BL, Dong RN, Bang YP, Li M. Haemostatic materials for wound healing applications. *NATURE REVIEWS CHEMISTRY* **5**, 773-791 (2021).
20. Cho Y, Beak JW, Sagong M, Ahn S, Nam JS, Kim ID. Electrospinning and nanofiber technology: fundamentals, innovations, and applications. *ADVANCED MATERIALS* **37**, (2025).
21. Roope LSJ*, et al.* The challenge of antimicrobial resistance: What economics can contribute. *SCIENCE* **364**, 41 (2019).
22. Kalelkar PP, Riddick M, García AJ. Biomaterial-based antimicrobial therapies for the treatment of bacterial infections. *NATURE REVIEWS MATERIALS* **7**, 39-54 (2022).
23. Huang XC*, et al.* A skin-interfaced three-dimensional closed-loop sensing and therapeutic electronic wound bandage. *NATURE COMMUNICATIONS* **16**, (2025).
24. Liu ZJ*, et al.* Wireless intelligent patch for closed-loop in situ wound management. *ADVANCED SCIENCE* **11**, (2024).

25. Ge ZY*, et al.* Wireless and closed-Loop smart dressing for exudate management and on-demand treatment of chronic wounds. *ADVANCED MATERIALS* **35**, (2023).
26. Liu L*, et al.* Highly elastic and strain sensing corn protein electrospun fibers for monitoring of wound healing. *ACS NANO* **17**, 9600-9610 (2023).
27. Wang LY*, et al.* Wound state monitoring by multiplexed, electrochemical, real-time, localized, inflammation-tracking nitric oxide sensor (MERLIN). *SCIENCE ADVANCES* **11**, (2025).
28. Lin X*, et al.* Ultra-conformable ionic skin with multi-modal sensing, broad-spectrum antimicrobial and regenerative capabilities for smart and expedited wound care. *ADVANCED SCIENCE* **8**, (2021).
29. Zhang XJ*, et al.* Janus nanofiber membranes with photothermal-enhanced biofluid drainage and sterilization for diabetic wounds. *ADVANCED FUNCTIONAL MATERIALS* **34**, (2024).
30. Zhang JY*, et al.* The solver of conflicting needs: research advances in Janus membranes for tissue engineering. *ADVANCED FUNCTIONAL MATERIALS*, (2025).
31. Yang YH*, et al.* Sprayable biomimetic double mask with rapid autophasing and hierarchical programming for scarless wound healing. *SCIENCE ADVANCES* **10**, (2024).
32. Ju Y*, et al.* Surface enzyme-polymerization endows Janus hydrogel tough adhesion and regenerative repair in penetrating orocutaneous fistulas. *NATURE COMMUNICATIONS* **15**, (2024).
33. Jin X*, et al.* Photothermal wood biopatch clears toxins and exudate to heal wounds. *ADVANCED FUNCTIONAL MATERIALS*, (2025).
34. Li B*, et al.* Photothermal therapy of tuberculosis using targeting pre-activated macrophage membrane-coated nanoparticles. *NATURE NANOTECHNOLOGY* **19**, (2024).
35. Wang JX*, et al.* A smart photothermal nanosystem with an intrinsic temperature-control mechanism for thermostatic treatment of bacterial infections. *ADVANCED MATERIALS* **34**, (2022).
36. Lou S*, et al.* Aggregation-induced emission-based nanoparticles for synergistic photothermal antibacterial therapy and anti-inflammatory regulation in periodontal infections. *ACS NANO*, (2025).
37. Su QW*, et al.* Strategies and applications of antibacterial surface-modified biomaterials. *BIOACTIVE MATERIALS* **53**, 114-140 (2025).
38. Su CH*, et al.* Enhancing microcirculation on multitriggering manner facilitates angiogenesis and collagen deposition on wound healing by photoreleased NO from hemin-derivatized colloids. *ACS NANO* **13**, 4290-4301 (2019).
39. Chen SW*, et al.* Transforming healthcare: intelligent wearable sensors empowered by smart materials and artificial intelligence. *ADVANCED MATERIALS* **37**, (2025).
40. Zhang HM, Landmann F, Zahreddine H, Rodriguez D, Koch M, Labouesse M. A tension-induced mechanotransduction pathway promotes epithelial morphogenesis. *NATURE* **471**, 99-U120 (2011).
41. Wei H, Jing HC, Cheng C, Liu YQ, Hao JC. A biomimetic one-stone-two-birds hydrogel with electroconductive, photothermally antibacterial and bioadhesive properties for skin tissue regeneration and mechanosensation restoration. *ADVANCED FUNCTIONAL MATERIALS* **35**, (2025).

42. Qu JW, *et al.* Natural tannin and upconversion photons co-potentiate Fe fenton anticancer therapy. *ADVANCED FUNCTIONAL MATERIALS*, (2025).
43. He WY, *et al.* Tannic acid-iron complex-based nanozyme ameliorates parkinson's disease via relieving oxidative stress and neuroinflammation. *ACS NANO* **19**, 33212-33229 (2025).
44. Han RH, *et al.* High Anti-Jamming Flexible Capacitive Pressure Sensors Based on Core-Shell Structured AgNWs@TiO2. *ADVANCED FUNCTIONAL MATERIALS* **33**, (2023).
45. Yuan Z, *et al.* Near-infrared light-triggered nitric-oxide-enhanced photodynamic therapy and low-temperature photothermal therapy for biofilm elimination. *ACS NANO* **14**, 3546-3562 (2020).
46. You YL, *et al.* Bacterial cell wall-specific nanomedicine for the elimination of Staphylococcus aureus and Pseudomonas aeruginosa through electron-mechanical intervention. *NATURE COMMUNICATIONS* **16**, (2025).
47. Chen M, *et al.* Photo-responsive nanozyme disrupts bacterial electron transport chain for enhanced anti-Biofilm therapy. *ADVANCED FUNCTIONAL MATERIALS* **35**, (2025).
48. Wu QQ, *et al.* Spermidine-functionalized injectable hydrogel reduces inflammation and enhances healing of acute and diabetic wounds in situ. *ADVANCED SCIENCE* **11**, (2024).

Figures

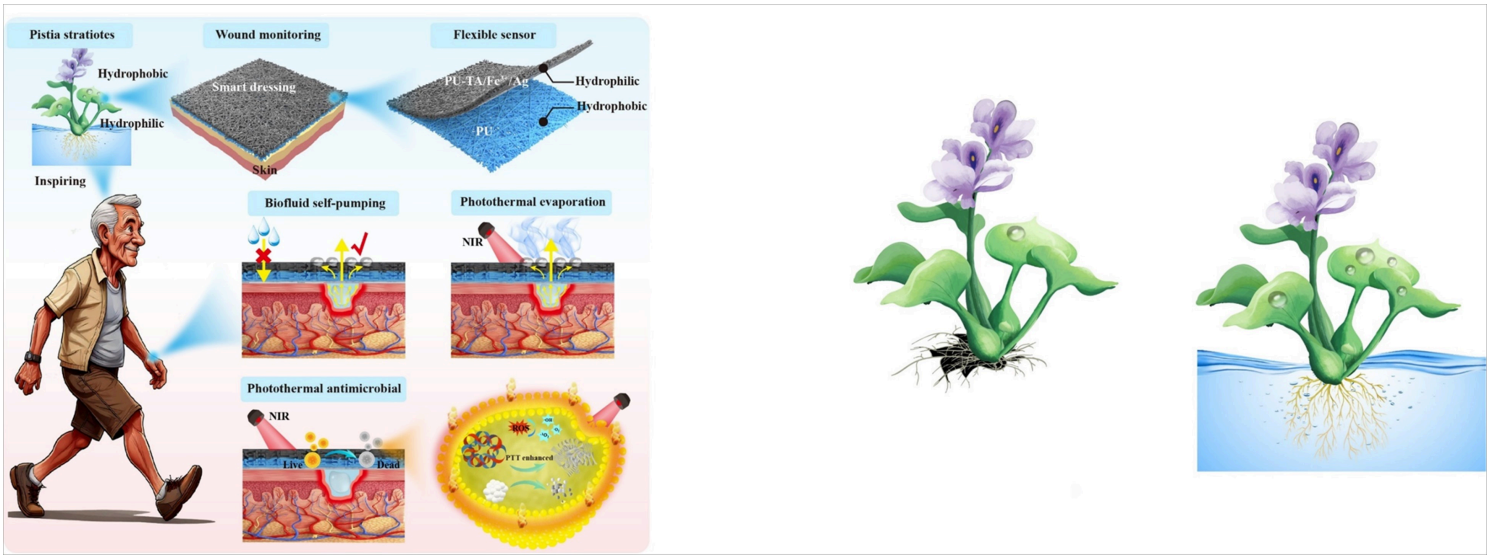

Figure 1

Material structure diagram and demonstration of liquid drainage and sterilization effect.

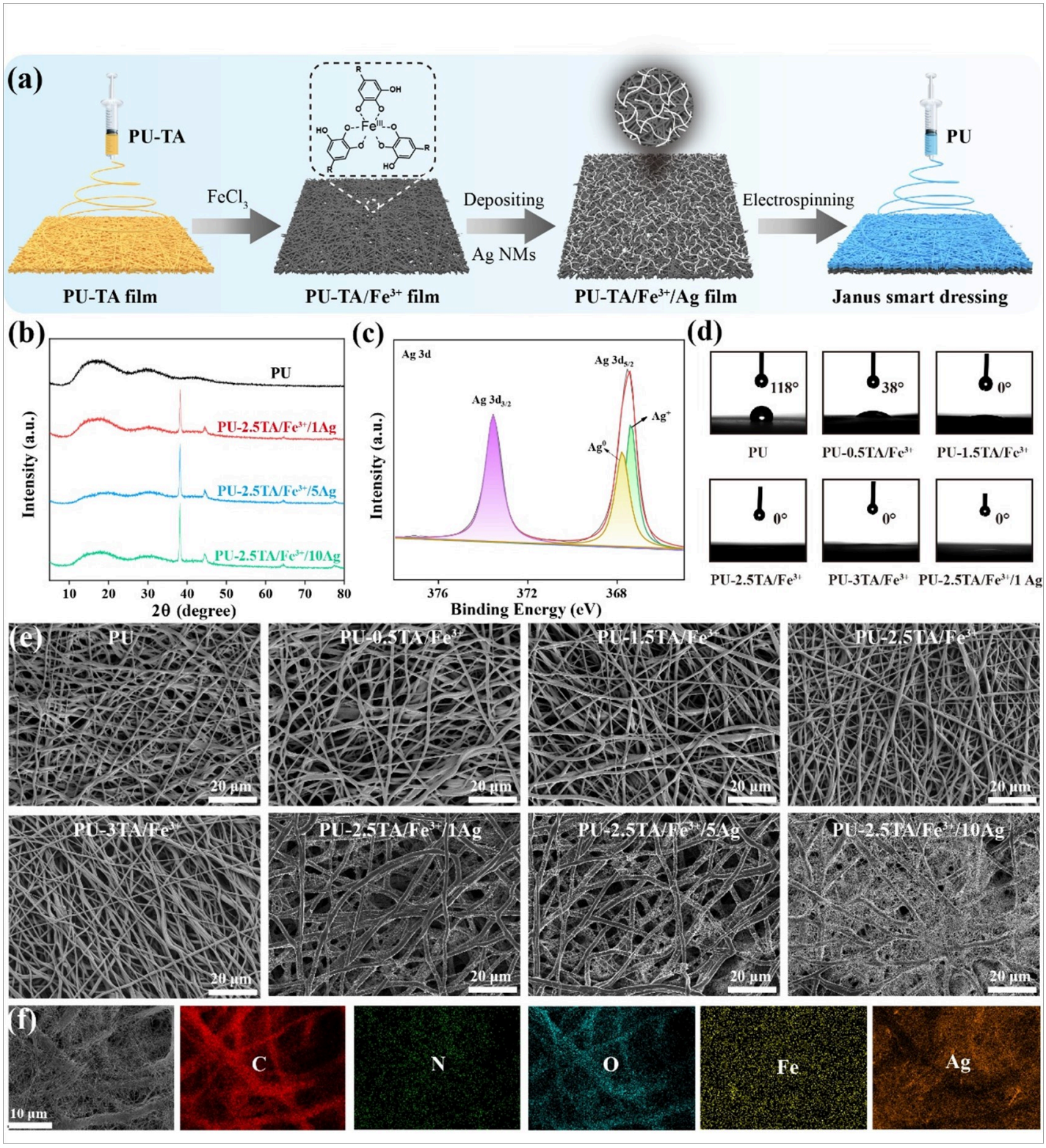

Figure 2

a) Schematic diagram of the process for preparing double-layer nanofiber membranes by electrospinning. (b) XRD patterns of PU and PU-2.5TA/Fe^{3+}/xAg (x=1, 5, 10) nanofiber membranes. (c) Ag 3d elemental XPS spectrum of the PU-2.5TA/Fe^{3+}/1Ag@PU Janus nanofiber membrane. (d) Water contact Angle tests for PU-xTA/Fe^{3+} (x=0, 0.5, 1.5, 2.5, 3) and PU-2.5TA/Fe^{3+}/1Ag nanofiber membranes.

(e) SEM images of five kinds of PU-xTA/Fe^{3+} (x=0, 0.5, 1.5, 2.5, 3) and three kinds of PU-2.5TA/Fe^{3+}/xAg (x=1, 5, 10) nanofiber membranes. (f) Elemental mapping diagrams of PU-2.5TA/Fe^{3+}/1Ag nanofiber membranes (C, N, O, Fe, Ag).

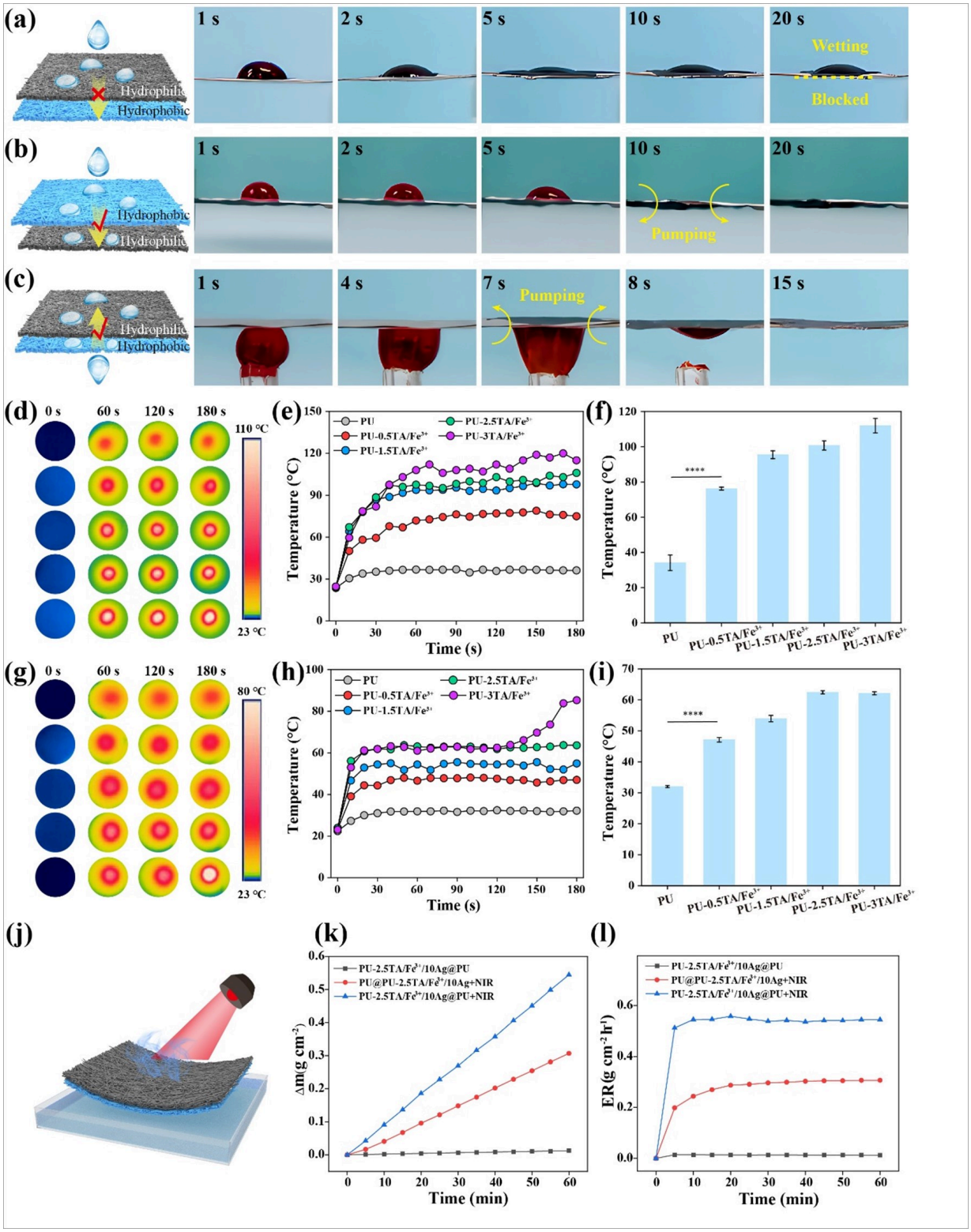

Figure 3

Demonstration diagram of the liquid conduction performance of PU-2.5TA/Fe^{3+}/10Ag@PU bilayer nanofiber membrane. (a) upper hydrophilic layer, lower hydrophobic layer; (b) upper hydrophobic layer, lower hydrophilic layer; (c) upper hydrophilic layer, lower hydrophobic layer. In the dry state, (d) the thermal imaging diagrams, (e) heating curves and (f) equilibrium temperature diagrams of PU-xTA/Fe^{3+} (x=0, 0.5, 1.5, 2.5, 3) nanofiber membranes under 808 nm NIR (1.5W/cm^2). (g, h, i) Correspond to the wet conditions. (j) Schematic diagram of photothermal evaporation. (k) Evaporation volume of ultrapure water from PU-xTA/Fe^{3+} nanofiber membranes. (l) Evaporation rate.

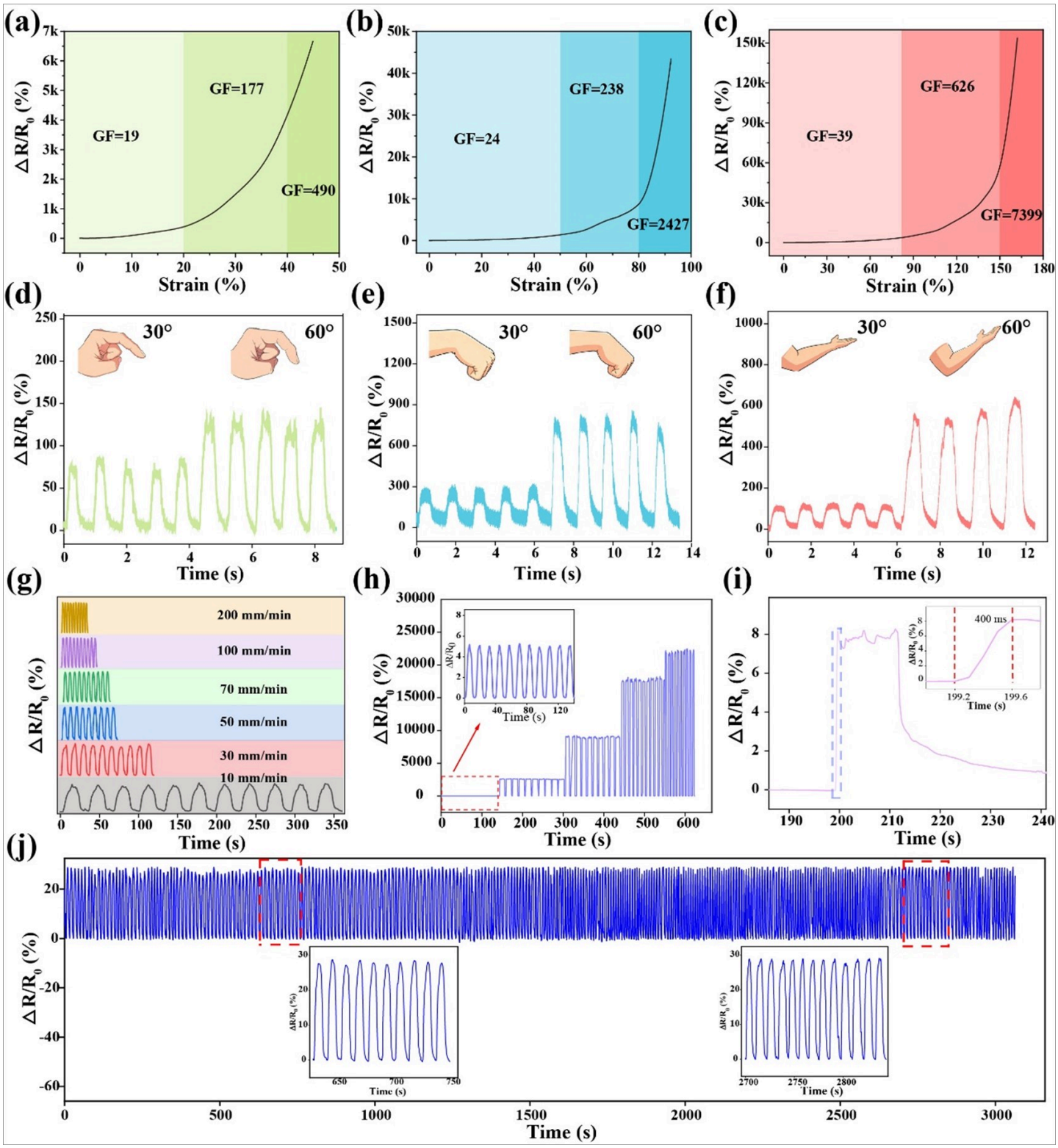

Figure 4

Strain sensing performance. (a-c) Relative change of resistance with effect of tensile strain of PU-2.5TA/Fe^{3+}/xAg (x=1, 5, 10) (d-f). The motion tracking of the finger, wrist, and elbow. (g) Effect of tensile velocity on the response stability of PU-2.5TA/Fe^{3+}/10Ag. (h) Effect of strain degree on the response stability of PU-2.5TA/Fe^{3+}/10Ag. (i) Response time of the smart scaffolds. (j) The relative change in resistance of the tension-release cycle test within 50 min at 10% strain.

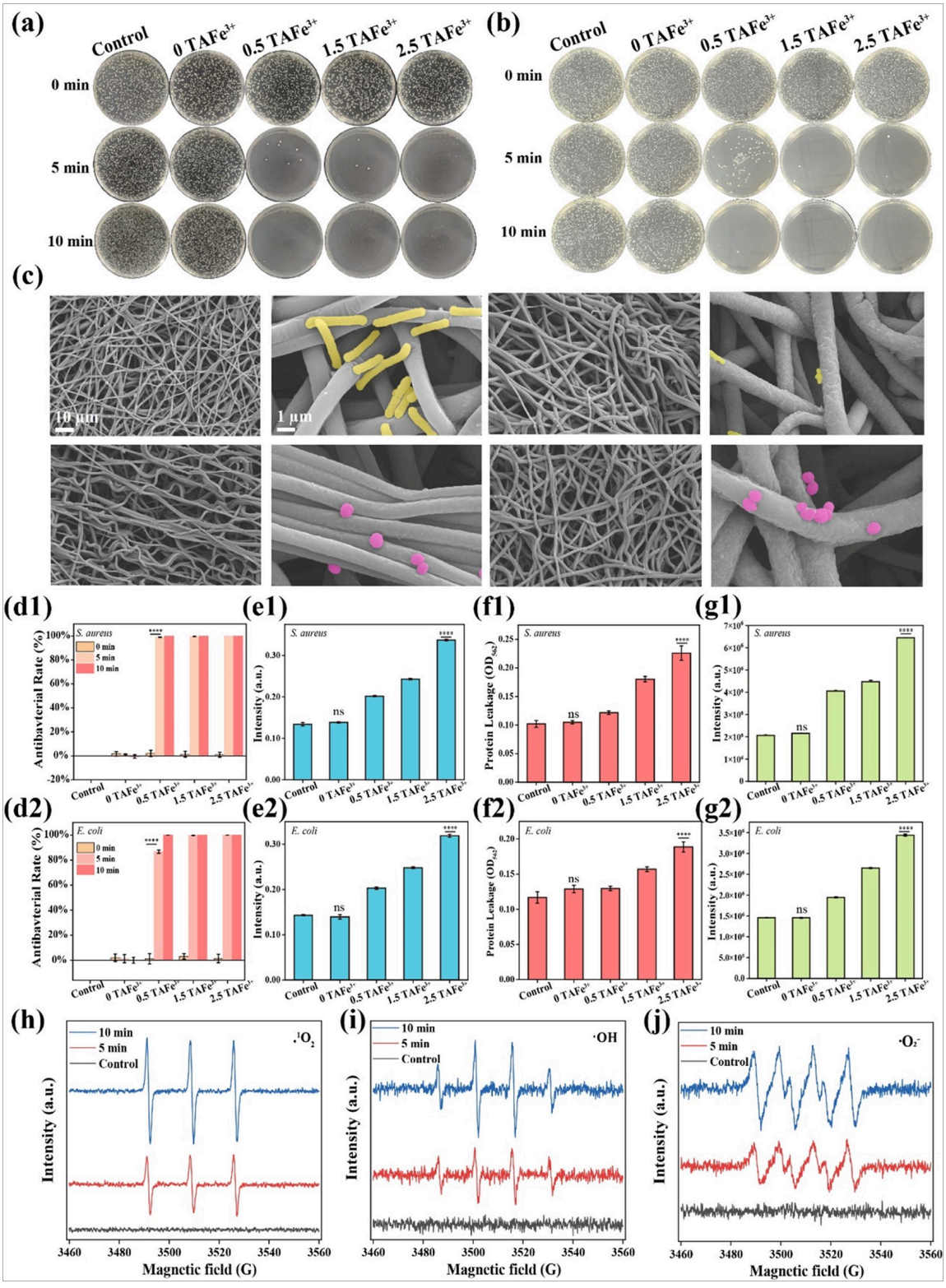

Figure 5

(a,b) The antibacterial effect of PU-xTA/Fe^{3+} (x=0, 0.5, 1.5, 2.5) nanofiber membrane on *S. aureus* and *E. coli*. (c) SEM antibacterial images (live bacteria in the control group and dead bacteria in the PU-2.5TA/Fe^{3+}+NIR treatment group, targeting *E. coli* and *S. aureus*). (d1, d2) The antibacterial rate against *S. aureus* and *E. coli*. (e1, e2) The changes in the permeability of cell membranes of *S. aureus* and *E. coli*. (f1, f2) protein leakage situation. (g1, g2) ROS levels. The intensities of (h) superoxide anion, (i) hydroxyl radical, and (j) singlet oxygen generated by PU-2.5%TA/Fe^{3+} nanofiber membranes under irradiation for 0 min, 5 min, and 10 min, respectively.

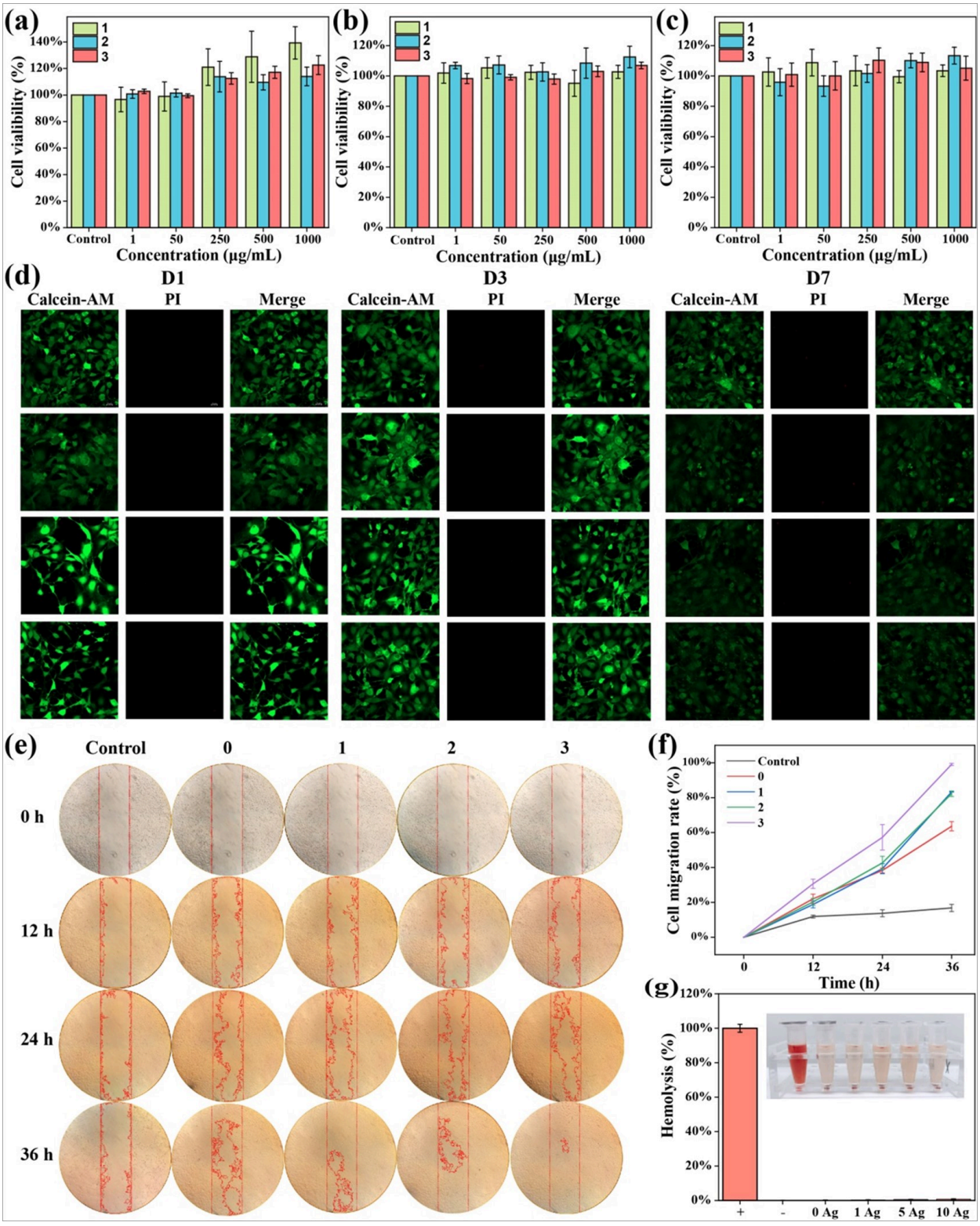

Figure 6

(a-c) PU-2.5TA/Fe^{3+}/xAg@PU (x=1, 5, 10) Janus nanofiber membrane cytotoxicity at 1, 3, 7 days. (d) Confocal microscopy images of Live/Dead fluorescence staining of cells on days 1, 3, and 7. (e) Cell scratch image results. (f) Cell migration rate. (g) Hemolysis rate of red blood cells in PU-2.5TA/Fe^{3+}/xAg@PU (x=0, 1, 5, 10) nanofiber membranes.

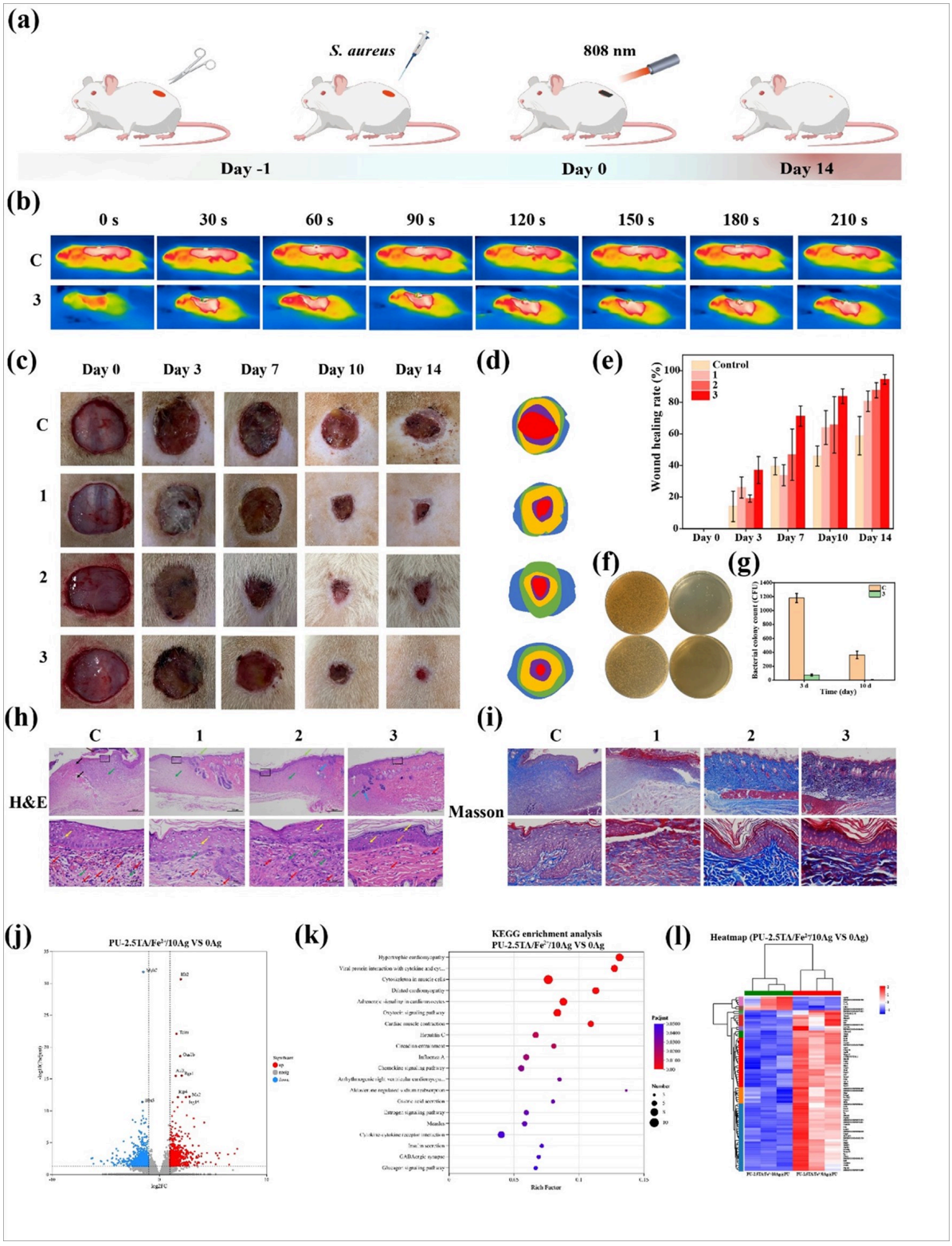

Figure 7

(a) Flowchart illustrating the construction process of the full-thickness skin defect model caused by Staphylococcus aureus infection. (b) Infrared thermal imaging images of rats in each experimental group after photothermal treatment. (c) Representative wound photos and (d) illustrations of the healing status of the treated wounds. (e) Comparison of wound repair rates among different treatment groups. (f) Results of wound exudate smear tests (on the 3rd and 10th days) and (g) quantitative analysis of the

corresponding antibacterial rates. (h) H&E staining results of the wound tissue after 14 days of treatment and (i) Masson staining results. (j) Volcano plots of differentially expressed genes (DEGs) in the PU-2.5TA/Fe^{3+}/10Ag@PU group and the PU-2.5TA/Fe^{3+}/0Ag@PU group on the 14th day. (k) KEGG enrichment analysis. (l) Heat map. (c, 1, 2, 3, correspond to Control, PU-2.5TA/Fe^{3+}, PU-2.5%TA/Fe^{3+}/0Ag@PU, PU-2.5TA/Fe^{3+}/10Ag@PU.)

Supplementary Files

This is a list of supplementary files associated with this preprint. Click to download.

- Figure8.mp4
- Figure9.mp4
- Figure10.mp4
- Supporting.docx